ADVANCED ELECTRONIC MATERIALS Open Access

www.advelectronicmat.de

High-Quality Epitaxial Five-Layer Aurivillius Films with In-Plane Ferroelectricity for Electrocaloric Cooling

Sara Lafuerza, Javier Blasco, Marco Evangelisti, Gloria Subías, David Gracia, José Á. Pardo, Eduardo Barriuso, Xavier Torrelles, Jessica Padilla-Pantoja, José M. Caicedo, and José Santiso**

High-quality purely *c*-axis oriented epitaxial thin films of the Aurivillius phase $Sr_2Bi_4Ti_5O_{18}$ with $n = 5$ $(Sr,Bi)TiO_3$ perovskite-like layers, are grown on $SrTiO_3$ substrates by pulsed laser deposition. The highest crystalline quality is obtained with a 20 wt.% Bi-excess target and average stacking order values in the proximity of the ideal value $n = 5$ are attained for an optimum deposition temperature of 650 °C. Scanning transmission electron microscopy reveals regions with n ranging from 4 to 6 around an average thickness of $n = 5$, in agreement with the X-ray diffraction analysis. Interdigital electrodes are used to probe the in-plane polarization and survey the electrocaloric properties. A maximum adiabatic temperature change of $\Delta T \sim 0.95$ °C for an electric field of 150 kV cm^{-1} is observed at ≈135 °C. Larger values are expected at higher temperatures around the ferroelectric Curie temperature, T_C. Since T_C of $Sr_2Bi_4Ti_5O_{18}$ can be tuned by codoping, the findings pave the way toward a large electrocaloric effect at ambient temperature.

1. Introduction

The electrocaloric effect (ECE) observed in solid-state ferroelectric materials presents an efficient and environmentally friendly alternative to the conventional vapor compression technology for refrigeration applications near room temperature.[1–4] Electrocaloric (EC) materials exhibit reversible adiabatic temperature (ΔT) and isothermal entropy (ΔS) changes, in response to electric field variations ΔE, enabling the development of a thermodynamic cycle suitable for either cooling or also heating applications. EC materials have been in the spotlight since the mid-2000s, following the observation of a giant ECE in a thin film of the perovskite oxide $PbZr_{0.95}Ti_{0.05}O_3$, reaching $\Delta T \sim 12$ °C (for $\Delta E = 480$ kV cm^{-1}) near its ferroelectric Curie temperature, $T_C \sim 222$ °C.[5] They are advantageous over the considerably more well-developed magnetocaloric materials because of the easier application and higher efficiency of E fields compared to magnetic fields, which makes EC coolers compact in volume and suitable for miniaturization. In the last years, an extraordinary evolution in the ΔT response has been reported, reaching up to 45 °C ($\Delta E = 598$ kV cm^{-1}) at room temperature in a Ba-doped $PbZrO_3$ thin film.[6] Besides, the predicted high efficiency of 60–70% in energy conversion has recently been experimentally demonstrated in an EC device based on a $PbSc_{0.5}Ta_{0.5}O_3$ multilayer capacitor.[7]

Ferroelectric thin films promote strong ΔT responses as they withstand higher E fields than bulk systems, since the latter are limited by electrochemical breakdown due to different microstructural imperfections (porosity, microcracks, etc.).[8] Besides, the small volume of thin films makes them particularly attractive for localized thermal management and hence they have a great potential for on-chip EC cooling of electronic devices (e.g., in data centers).[3,9] To date, as shown by the previously mentioned examples, the largest ΔT values have mainly been obtained in lead-containing perovskite thin films.[10] However, the use of toxic lead poses environmental barriers toward implementing widespread cooling and heating applications. In line with European directives,[11] hazardous lead must be avoided. Thus, progressing in the field of EC cooling urges the need of developing lead-free potential refrigerant materials.

S. Lafuerza, J. Blasco, M. Evangelisti, G. Subías, D. Gracia, J. Á. Pardo, E. Barriuso
Instituto de Nanociencia y Materiales de Aragón (INMA)
CSIC-Universidad de Zaragoza
Zaragoza 50009, Spain
E-mail: lafuerza@unizar.es

S. Lafuerza, J. Blasco, M. Evangelisti, G. Subías, D. Gracia
Departamento de Física de la Materia Condensada
Universidad de Zaragoza
Zaragoza 50009, Spain

J. Á. Pardo
Departamento de Ciencia y Tecnología de Materiales y Fluidos
Universidad de Zaragoza
Zaragoza 50018, Spain

X. Torrelles
Institut de Ciència de Materials de Barcelona (ICMAB-CSIC)
Campus UAB
Bellaterra, Barcelona 08193, Spain

J. Padilla-Pantoja, J. M. Caicedo, J. Santiso
Catalan Institute of Nanoscience and Nanotechnology (ICN2)
Campus UAB
Bellaterra, Barcelona 08193, Spain
E-mail: jose.santiso@icn2.cat

The ORCID identification number(s) for the author(s) of this article can be found under https://doi.org/10.1002/aelm.202400962

DOI: 10.1002/aelm.202400962

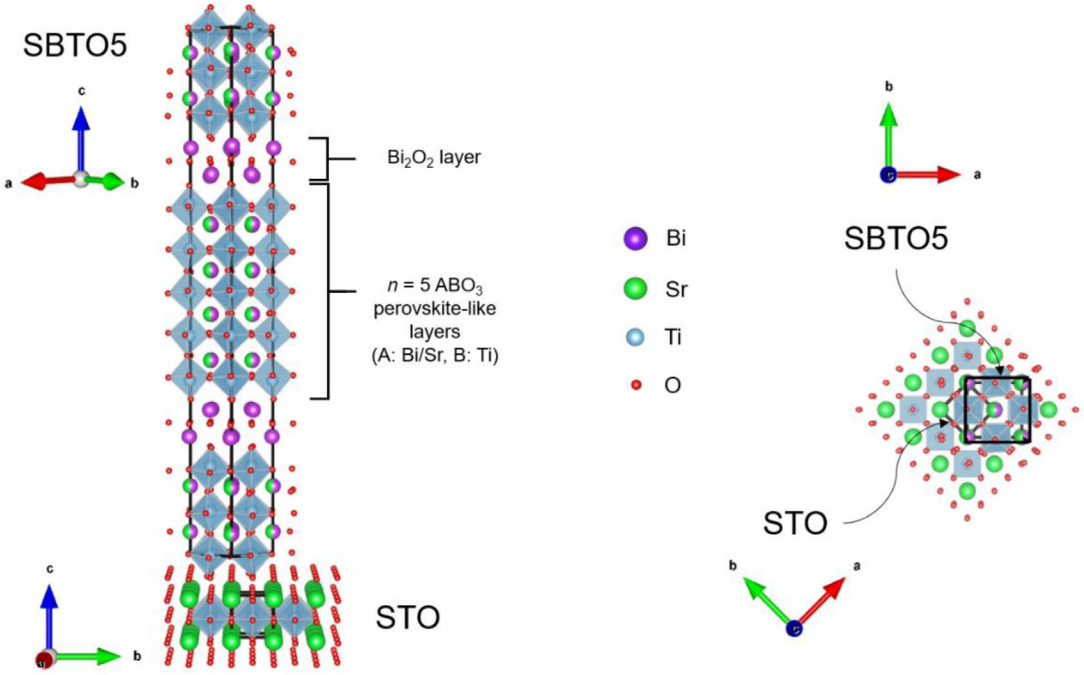

Figure 1. Schematic of the $n = 5$ Aurivillius phase $Sr_2Bi_4Ti_5O_{18}$ (SBTO5) unit cell in relation to that of the $SrTiO_3$ (STO) substrate along two different views: lateral (left) and top (right). SBTO5 has an orthorhombic crystal structure (*B2cb* space group) at room temperature, which is nearly tetragonal with $a \sim b \approx 5.46$ Å, being $c \approx 48.85$ Å.[27] The lattice parameter of SBTO5 assuming a pseudotetragonal structure is 3.861 Å, which shows a small ≈1% mismatch with the lattice constant of cubic STO ($a = 3.905$ Å) and favors the growth of the Aurivillius phase with the in-plane lattice parameter along the [110] direction on the STO surface. Figure prepared with VESTA.[28]

Lead-free Aurivillius phases with general chemical formula $Bi_2A_{n-1}B_nO_{3(n+1)}$, also known as bismuth layered structure ferroelectrics, have been recognized as promising candidates for EC cooling because of their high dielectric strength, low leakage current and endurance upon E field cycling.[1,12,13] They are composed by n perovskite-like layers $(A_{n-1}B_nO_{3n+1})^{2-}$ sandwiched between bismuth oxide layers $(Bi_2O_2)^{2+}$ along the c-axis, being the c cell parameter much larger than a and b (**Figure 1**). The high-temperature crystal structure in the paraelectric phase is tetragonal (*I4/mmm* space group). Complex polar structures, typically orthorhombic ($A2_1am$ space group for even n, *B2cb* space group for odd n), which involve not only the B-cation like in $BaTiO_3$ and other simple perovskites but also the A-cation and oxygens, originate below T_C.[1,11,14] The layered structure of Aurivillius phases results in highly anisotropic electrical properties, with a quasi 2D polarization lying in the *ab* plane.[15] More specifically, in the orthorhombic structures ($A2_1am$ and *B2cb* space groups) the polarization lies entirely along the a-axis.[16]

Despite their potential for EC thermal control applications, the ECE of Aurivillius oxides remains largely unexplored. The few dedicated studies primarily focused on three-layer ($n = 3$) Aurivillius compositions with Nb and/or Ta at the B-site. Given the inherently high T_C values of Aurivillius phases, chemical substitutions were applied in bulk $n = 3$ Aurivillius phases to adjust T_C, and thereby optimize the ECE,[17] closer to room temperature. For instance, $SrBi_2(Nb_{0.2}Ta_{0.8})_2O_9$ was investigated with Pr^{3+} and Ba^{2+} doping separately,[18–20] yielding maximum ΔT values of ≈0.5 °C ($\Delta E = 55$ kV cm^{-1}) and ≈0.8 °C ($\Delta E = 50$ kV cm^{-1}), respectively, near 140 °C. Lower-temperature ECE peaks were obtained in $SrBi_{1.98}La_{0.02}Nb_{2-x}Ta_xO_9$ ($x = 0.5$, 1.0, 1.5) compositions,[21] though with much smaller ΔT values of ≈0.005 °C ($\Delta E = 35$ kV cm^{-1}). The only study of EC properties in Aurivillius thin films reported a large $\Delta T \sim 5$ °C ($\Delta E = 600$ kV cm^{-1}) in a polycrystalline film of $SrBi_2Ta_2O_9$ around its $T_C \sim 290$ °C.[22]

Encouraged by the trend of decreasing T_C values upon increasing the number of perovskite-like layers in the B = Ti Aurivillius family $Sr_{n-3}Bi_4Ti_nO_{3n+3}$ (with T_C values of 675, 520 and 285 °C for $n = 3$, 4 and 5, respectively),[23] we recently investigated the EC properties of the lowest T_C member, five-layer $Sr_2Bi_4Ti_5O_{18}$, in its bulk form. By employing La/Nb codoping, we could tune the ECE near room temperature, reaching a maximum $\Delta T \sim 0.3$ °C ($\Delta E = 37$ kV cm^{-1}) at 80 °C for the optimum composition $Sr_2Bi_{3.44}La_{0.5}Ti_{4.8}Nb_{0.2}O_{18}$.[24] Building on these findings, the next step to enhance the EC performance of these materials is to fabricate them in thin-film form, aiming for a higher dielectric strength and thus stronger ECE.[8] Given the complexity of these five-layer Aurivillius phases in terms of both composition and structure, a reasonable approach is to tackle first the investigation of the parent compound, $Sr_2Bi_4Ti_5O_{18}$ (hereinafter denoted SBTO5). We also note that, in the general Aurivillius family $Sr_{n-3}Bi_4Ti_nO_{3n+3}$, there is a dependence of the ferroelectric remanent polarization on the parity of n, as reported in previous works on bulk[25] and thin-film[26] forms, with polarization values being larger for odd n than for even n. The primary motivation for selecting the $n = 5$ Aurivillius phase SBTO5 over the less complex lower-n analogues lies in a balance between T_C and polarization

values, considering the target cooling applications near ambient temperature.

The $n = 5$ SBTO5 Aurivillius phase exhibits an orthorhombic structure with space group *B2cb* at room temperature (Figure 1), and thus its ferroelectric polarization lies entirely along the *a*-axis. The high anisotropy in its electrical properties makes the fabrication of single-crystalline epitaxial thin films particularly appealing, as these can potentially yield a greater polarization response than randomly oriented polycrystalline thin films. As compared to *a*- and *b*-axis oriented epitaxial Aurivillius films, *c*-axis oriented films are generally easier to produce due to the favorable structural matching with the *ab*-plane of commercial perovskite single crystals. Nevertheless, achieving high-quality epitaxial Aurivillius films is challenging due to several difficulties. First, the precise control of the Bi composition is complicated by the high deposition temperatures required for epitaxial growth and the volatility of Bi-containing compounds. Second, the wide compositional variation along the *c*-axis can lead to the formation of structural defects, such as out-of-phase boundaries (OPBs) or the intergrowth of other-*n* Aurivillius phases.[16,29–32] Furthermore, *c*-axis oriented epitaxial Aurivillius films face the limitation that standard bottom-top electrode configurations cannot probe the in-plane polarization.

Herein, we first present the optimization of the growth conditions for high-quality SBTO5 Aurivillius epitaxial thin films, which we grow on [001]-oriented $SrTiO_3$ (STO) single-crystal substrates through pulsed laser deposition (PLD). Assuming a pseudotetragonal structure, the lattice parameter of SBTO5 is 3.861 Å, which shows a small ≈1% mismatch with the lattice constant of cubic STO ($a = 3.905$ Å), facilitating cube-on-cube growth of the corresponding perovskite-like blocks. That is, the Aurivillius phase grows with the in-plane *a*- and *b*-axes aligned along the [110] directions on the STO surface (Figure 1). To counteract Bi volatility, dense ceramic targets containing 10 and 20 wt.% excess of the Bi_2O_3 precursor were used. In addition, we examined deposition temperature (T_{dep}) values in the range 650 – 800 °C. We subsequently investigated the in-plane ferroelectric and EC properties of the resultant films using top interdigital electrodes (IDEs), fabricated by optical lithography and Cr/Au evaporation. We note that the experimental investigations into the EC properties of epitaxial thin films are rare, particularly those utilizing non-standard planar electrode geometries like IDEs.[33,34] In the present Aurivillius films, the IDEs have facilitated the observation of well-saturated remanent hysteresis loops at room temperature, confirming the presence of ferroelectricity and yielding a maximum ECE response of $\Delta T \sim 0.95$ °C ($\Delta E = 150$ kV cm^{-1}) at ≈135 °C. Notably, this exceeds the maximum ΔT response previously achieved in bulk SBTO5 upon doping, which was only ≈0.27 °C ($\Delta E = 37$ kV cm^{-1}) at ≈80 °C.[24] While this performance may be considered moderate compared to the giant ECE values reported for other ferroelectric perovskite thin films,[9,35] we anticipate that a significantly higher ECE could be realized at temperatures closer to T_C. This work also provides insights on critical considerations when using IDEs for assessing the ferroelectric and EC properties of epitaxial thin films, particularly regarding the substrate material selection and its impact on the electrical properties of the films.

2. Results and Discussion

Several thin films of the two available targets were fabricated at different T_{dep} values in order to find the optimum growth conditions leading to high-quality *c*-axis oriented epitaxial SBTO5 (see Table S1, Supporting Information for a full detailed list, and Figure S1, Supporting Information for a selection of X-ray reflectivity data). We first focused on the lowest Bi-excess target, 10 wt.% SBTO5. **Figure 2**a shows the X-ray diffraction (XRD) patterns of the films deposited at T_{dep} equal to 650, 750 and 800 °C. At first inspection of the full diffractograms, only 0 0 *l* reflections with even *l* values besides the STO reflections are detected, which is compatible with single-phase and highly *c*-axis oriented epitaxial SBTO5 Aurivillius films. No trace of a different orientation was detected. Regarding the evolution upon increasing T_{dep}, the high crystalline quality evident from the narrow peaks in the patterns corresponding to 650 and 750 °C, gets significantly worse at 800 °C. Concerning the surface morphology of these samples, a reasonably low root mean square roughness value ≤ 2–3 nm was derived for all the films from the 1 μm × 1 μm size atomic force microscopy (AFM) topography scans (see Figure S2, Supporting Information). However, the uniform and dense granular structure obtained for 650 and 750 °C shows an additional distribution of islands for 800 °C. Based on the similarity with the distribution of cuboids detected at early stages of growth in related epitaxial $n = 4$ $Bi_5FeTi_3O_{15}$ films,[30] we speculate that the islands observed in the highest deposition temperature film could be due to an improper coalescence of the perovskite slabs due to defects like OPBs. Regarding the 20 wt.% SBTO5 target, and taking the previous conclusion as a starting point, an intermediate T_{dep} value of 700 °C was checked, as the value of 800 °C was considered too high to yield high-quality films. Figure 2b shows the XRD patterns of the films deposited at T_{dep} equal to 650, 700, and 750 °C from the highest Bi-excess target. In this case, all the films seem single-phase and highly *c*-axis oriented with a more comparable high crystalline quality among them, being the pattern corresponding to 650 °C the one showing the sharpest peaks.

Having achieved this high-quality of SBTO5 Aurivillius films allows us to extract further quantitative information from the XRD data and establish an optimum T_{dep}. Upon closer inspection of the XRD patterns in the detail regions shown in Figure 2a,b, in addition to the presence of a minor secondary phase indicated with # symbol (δ-Bi_2O_3 bixbyite), one can observe that some of the 0 0 *l* peaks shift to either higher or lower angles between films, which is a sign of intermixing of regions along the *c*-axis with periodicities deviating from the nominal $n = 5$ stacking order.[36] This intermixing is further evidenced by the doubling of certain particular peaks (i.e., 0 0 6, 0 0 18, 0 0 30 and 0 0 42) in some of the films deposited from both targets. Following the same methodology as described in ref.[36] we have derived the average stacking order n_{av} achieved in each film from the relative displacements between adjacent peaks in the diffractogram using the following general expression: $n_{av} = \frac{12}{l} \times [Q_l/(Q_l - Q_{l-2})] - 1$, applied to a representative subset of reflections with $l = 12$, 24, 36 and 48, in relation to the corresponding set l-2 = 10, 22, 34 and 46. **Figure 3** shows the representation of the n_{av} parameter versus T_{dep} for the films grown with the 10 wt.% and 20 wt.% targets separately. In addition, we have also included the information from the full width at half maximum (FWHM) of the peak

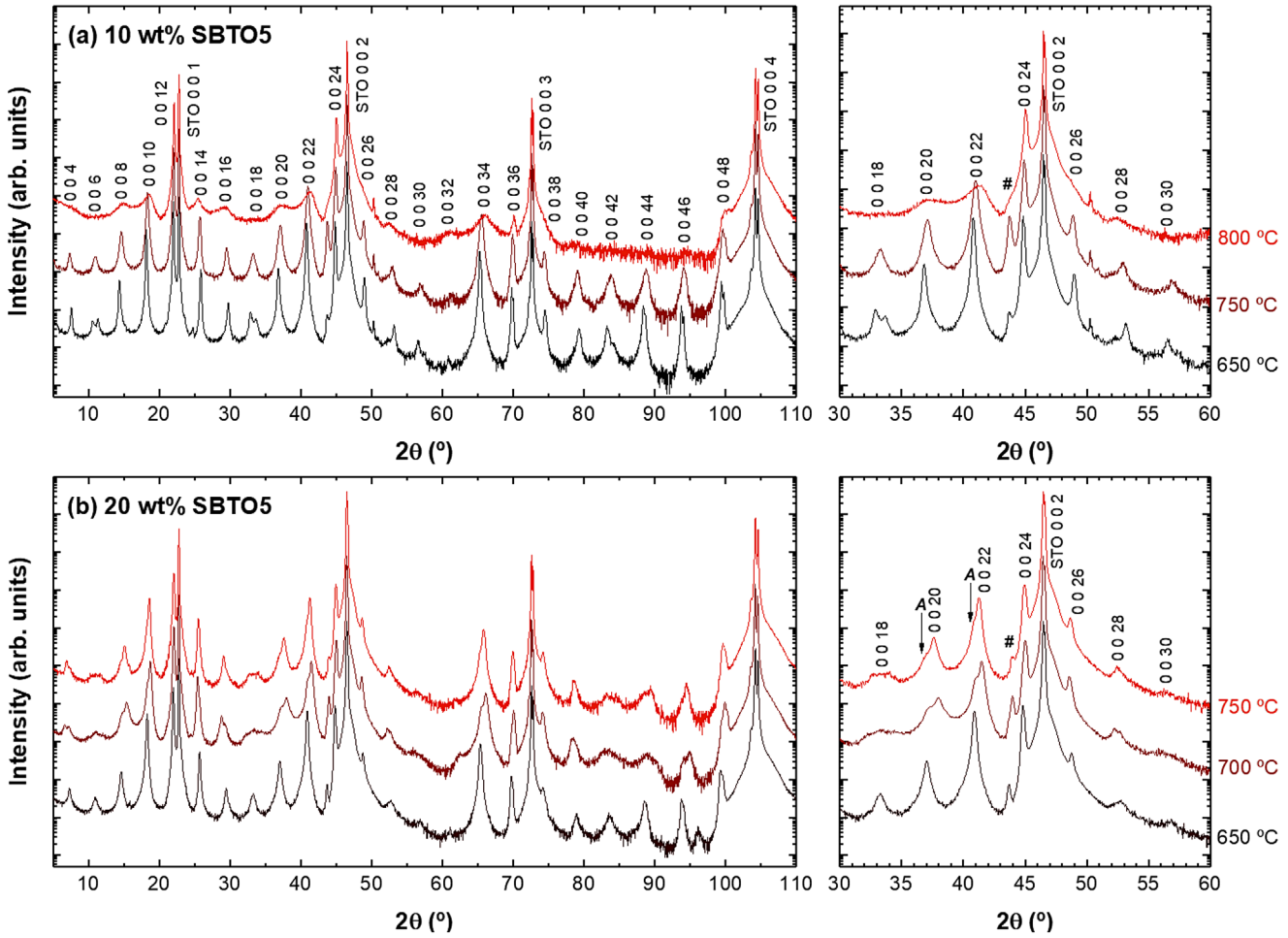

Figure 2. θ-2θ X-ray diffraction full patterns (left) and detail regions (right) of selected films grown using the (a) 10 wt.% and (b) 20 wt.% SBTO5 targets as a function of deposition temperature. In panels showing a detail region (right), # symbol indicates δ-Bi_2O_3 bixbyite secondary phase and *A*: other-n Aurivillius phase.

corresponding to reflection 0 0 22, as an indicator of the degree of crystallinity. First, the dispersion obtained in the n_{av} values is especially significant in the case of the 10 wt.% target, which we ascribe to fluctuations in Bi-content even between samples deposited in the same conditions. At the same time, looking at the FWHM values, we can conclude that the optimum temperature that leads to n_{av} closest to $n = 5$ together with the best crystallinity (i.e., lowest FWHM) is 650 °C for both 10 wt.% and 20 wt.% targets, although the derived n_{av} values are significantly better for the 20 wt.% target. As expected, increasing further T_{dep} leads to larger n_{av} values for both targets (higher in the case of the 20 wt.% target), and thus a decrease of the Bi-content in the films. We note that, although for the 10 wt.% target the increase in T_{dep} seems to yield n_{av} values in the proximity of $n = 5$, this is at the same time detrimental for the crystallinity, since the FWHM values increase above 0.3 °for this target. Further analysis from the peak positions in the XRD data in terms of the deviation of the interplanar distance with respect to the nominal value and the derivation of an average *c*-axis parameter is provided in Figures S3 and S4 (Supporting Information) respectively. The evolution of the average *c*-axis parameter versus n_{av} follows a trend consistent with lower Bi-content for higher n_{av} values as expected.

In the view of all these empirical results from the XRD analysis, we therefore conclude that the optimum growth conditions are obtained with the 20 wt.% Bi-excess target, which yields the highest crystalline quality and the n_{av} values in closest proximity to the ideal $n = 5$ periodicity at $T_{dep} = 650$ °C. In these films, the measured *c*-axis parameters are in the range 48.4 – 48.6 Å (see Figure S4, Supporting Information). Taking the average value 48.5 Å, this gives a small contraction in the *c*-axis direction of ≈-0.7% with respect to the reported bulk structure where $c = 48.85$ Å,[27] which is in consistency with the elastic response expected from the in-plane tensile strain of ≈+1.1%. Hence, SBTO5 films grown in these optimal conditions are of remarkable high-quality in terms of both crystallinity and degree of epitaxy. The high crystallinity is also demonstrated by the presence of Laue oscillations in the XRD pattern as shown for instance around the 0 0 12 reflection in **Figure 4**. Moreover, a high degree of epitaxy is deduced from the positions of the SBTO5 and STO reflections in the reciprocal space maps (RSMs). **Figure 5** presents the RSMs measured

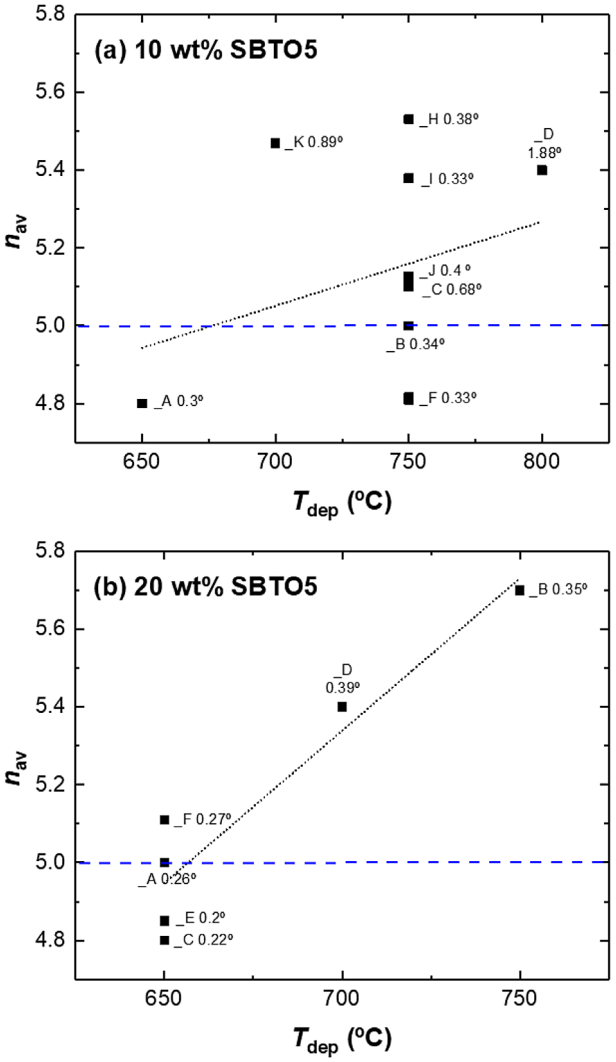

Figure 3. Calculated average stacking number *n* parameter from the XRD data versus the deposition temperature for selected films grown using the a) 10 wt.% and b) 20 wt.% SBTO5 targets. The dotted lines indicate the results of the linear regression, while horizontal blue dashed lines indicate the ideal $n = 5$ value. Next to each symbol, it appears indicated a label related to the sample name (Table S1, Supporting Information) followed by the value of the full width at half maximum of a selected diffraction peak as described in the text.

around STO 3 0 3 and 1 1 3 peaks ($\phi = 0$ and 45°, respectively) where the Q_x positions of the corresponding SBTO5 reflections, 3 3 *l* with odd *l* and 3 0 *l* with even *l* respectively, are in perfect coincidence, showing that the film is fully strained in-plane. Furthermore, the absence of a visible peak splitting in the RSMs indicates that we do not detect a differentiation between the orthorhombic *a* and *b* in-plane lattice parameters, which can be ascribed to a tetragonal structure in the film due to the strain or also to the presence of nanometer-size *a-b* crystal twining, which makes it difficult to be resolved with standard lab diffractometers.

The crystal quality of optimized films was also assessed by high-angle annular dark-field scanning transmission electron microscopy (STEM-HAADF) cross-section images as shown in **Figure 6**. The film deposited under optimized conditions shows a clear layered structure with the pure *c*-axis orientation. Neither secondary phases nor domains with different orientations were observed in the analyzed regions. As it can be observed in Figure 6a, the interface with STO substrate is sharp, while top surface morphology shows roughness of ≈2–3 nm, in consistency with the AFM analysis. The atomic resolution of the image evidences the sequence of the double Bi_2O_2 layers and (Sr,Bi)TiO_3 perovskite blocks along the growth direction parallel to *c*-axis. The higher magnification image of one zone of the SBTO5 film in Figure 6b shows the presence of a large density of stacking faults, indicated with yellow arrows, which interrupt the continuity of the Bi_2O_2 layers in the horizontal direction forming well defined steps in the vertical direction. The continuity of the perovskite layers in the lateral direction is not affected. Therefore, the stacking defects can be considered as OPBs consisting of one single perovskite cell translation of the structure in the *c*-axis direction, as often observed in Aurivillius-type structures.[29,32] The regions between these OPBs define slabs with an integer number of perovskite blocks ranging from 4 to 6, around an average thickness of $n = 5$, in agreement with the n_{av} parameter value derived from the XRD analysis in the same film. In the zone axis orientation of the cut, parallel to the [100]/[010] directions of the STO substrate, the perovskite blocks are equally oriented, which indicates a fully coherent growth of the film. The presence of the Bi_2O_2 layers produces a change in the stacking sequence of the perovskite blocks with an in-plane one-half-perovskite unit translation along the [100] direction, irrespectively of the *n* number of the perovskite slab, as expected for the Aurivillius-type structure. Altogether, this preserves the monolithic structure of the film despite the presence of the OPB defects. These OPBs do not seem to be related to any step in the substrate surface, and are probably generated by local fluctuations of the Bi-concentration during film growth, at least in the early stages.

Next, we evaluate the ferroelectric and EC properties in a selection of our high-quality *c*-axis oriented epitaxial SBTO5 Aurivillius films grown using the 20 wt.% Bi-excess target. In particular those with n_{av} in the vicinity of the $n = 5$ ideal value, and having different thicknesses: 74 nm ($n_{av} = 5.0$), ≈250 nm ($n_{av} = 4.8$) and 40 nm ($n_{av} = 5.4$), namely samples SBTO5_20_A, SBTO5_20_C and SBTO5_20_D, respectively, in Table S1 (Supporting Information). The assigned thickness value is deduced from the corresponding X-ray reflectivity (XRR) measurements except for the thickest sample, whose thickness was assumed from a rough estimation of the growth rate as to 0.1 nm per pulse following the results from XRR in a very thin sample (Figure S1, Supporting Information). Standard hysteresis measurements (Figure S5, Supporting Information) yield very large polarization values at high *E* field amplitudes, particularly for thinner films, while a distinct ferroelectric opening is only detected for the thickest film. This is likely attributed to the influence of the linear dielectric contribution from the STO substrate on the measured polarization, which becomes increasingly significant with thinner films. Due to potential substrate effects, the electrical measurements using surface IDEs are more complex than those with bottom-top electrode configurations, especially when interacting with a high-permittivity material such as STO.[37–40] A useful approach to effectively differentiate the intrinsic ferroelectric contributions in thin films, is the application of the remanent hysteresis

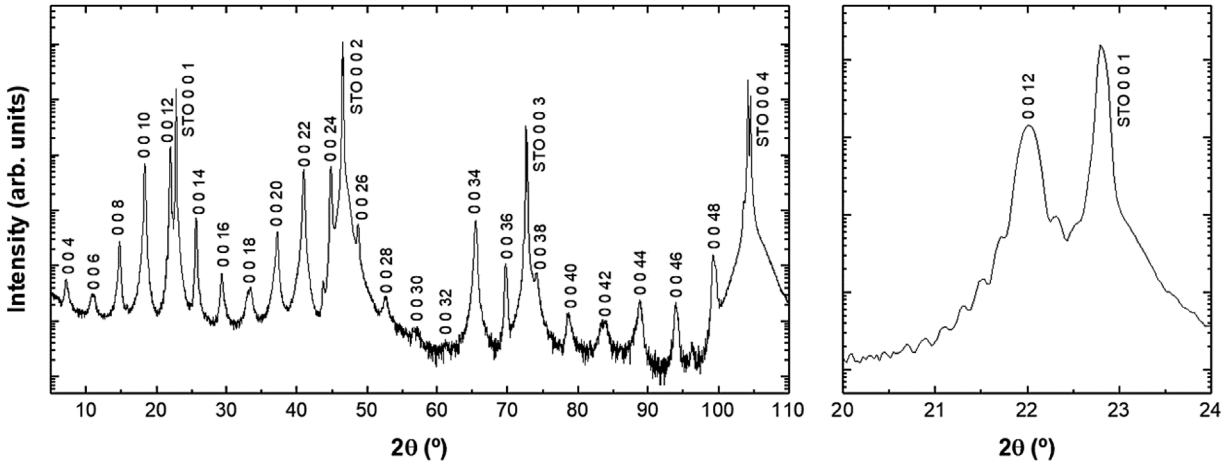

Figure 4. θ-2θ X-ray diffraction full pattern (left) and detail region (right) of a film grown in optimal conditions using the 20 wt.% SBTO5 target and deposition temperature T_{dep} = 650 °C (sample SBTO5_20_F, see Table S1, Supporting Information), illustrating the presence of Laue oscillations around the SBTO5 peaks in agreement with a thickness of 46 nm.

protocol based on the well-known PUND method.[41] This approach enables the separation of switching polarization (i.e., the film intrinsic ferroelectric polarization) from non-switching polarization (i.e., linear dielectric contributions and leakage currents). Further details about the remanent hysteresis protocol are given in Figure S6 (Supporting Information).

Figure 7 shows the $P(E)$ results at room temperature, derived from remanent hysteresis measurements on the selected films with an E field amplitude E_0 = 150 kV cm^{-1}. We observe clear hysteresis loops that confirm an intrinsic in-plane ferroelectricity in the selected SBTO5 Aurivillius films. Switching coercive fields E_C ≈60 kV cm^{-1} and zero-field remanent polarization P_r ≈6–8 μC cm^{-2} are found without evident systematic dependence on the film thickness or n_{av}. We note that the presence of intergrowths revealed by the STEM-HAADF images can affect the ferroelectric properties in the following ways: i) disruption of the long-range order of dipoles caused by the structural and compositional disorder, leading to reduced polarization and pinning effects that hinder the motion of ferroelectric domain walls, resulting in an increased E_C, as well as local strain fields and distortions that can either enhance or weaken the polarization; and ii) given the dependence of the polarization on the parity of n in the general Aurivillius family $Sr_{n-3}Bi_4Ti_nO_{3n+3}$, with polarization values being larger for odd n than for even n, a reduced polarization could be expected in films with $n_{av} < 5$ or $n_{av} > 5$, following the trend of P_r as a function of n.[26] In general, we observe larger polarization values in films where $n_{av} \geq 5$, while slightly smaller values are found in films with $n_{av} < 5$. The polarization curve of a thick sample grown using the 10 wt.% SBTO5 target (thickness ≈200 nm, n_{av} = 4.8) agrees reasonably well with the analogous film using the 20 wt.% target, as shown in Figure S7 (Supporting Information). Moreover, we observe a higher E_C magnitude compared to previous works in both thin-film[42,43] and bulk[24,25] forms, which is slightly larger for films with $n_{av} < 5$ or $n_{av} > 5$. Therefore, our results indicate a clear effect of the structural and compositional disorder on the ferroelectric properties, with a resulting polarization that cannot be simply predicted by the expected polarization values for a given n. This is also consistent with the disorder in the distribution of intergrowths, as identified by STEM-HAADF. Despite the presence of intergrowths, it is remarkable that our P_r values measured using surface IDEs exceed those previously reported for c-axis oriented epitaxial SBTO5 films probed using standard bottom-top electrodes and E fields up to 200 kV cm^{-1} (≈5 μC cm^{-2} for Pt/SBTO5/Pt and ≈0.9 μC cm^{-2} for Pt/SBTO5/$SrRuO_3$)[42] or even up to 400 kV cm^{-1} (≈2.5 μC cm^{-2} for Pt/SBTO5/$LaNiO_3$/$LaAlO_3$).[43] Additionally, our measurements reveal well-saturated hysteresis loops, unlike the reported $P(E)$ curves measured with bottom-top electrodes (E_C ≈50 kV cm^{-1}).[42,43]

We also observe that, the thinner the sample, the noisier the remanent hysteresis curve appears (Figure 7). This can be anticipated since it represents a small fraction of the total measured polarization. For this reason, we next focus on the film with the

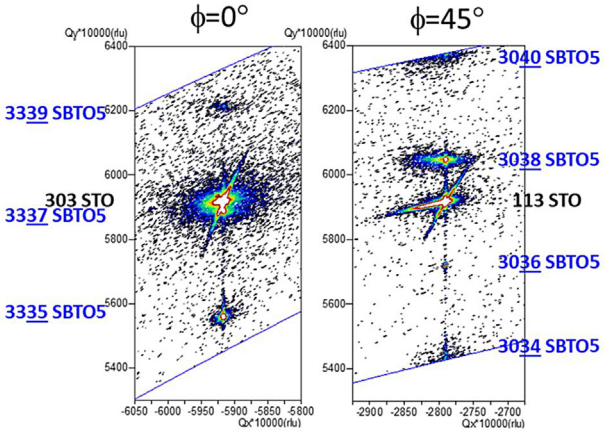

Figure 5. Reciprocal space maps around STO 3 0 3 (right) and 1 1 3 (left) peaks of a film grown in optimal conditions using the 20 wt.% SBTO5 target and deposition temperature T_{dep} = 650 °C (sample SBTO5_20_E, see Table S1, Supporting Information). The perfect coincidence of Q_x values between SBTO5 film and STO substrate shows that the film is fully strained.

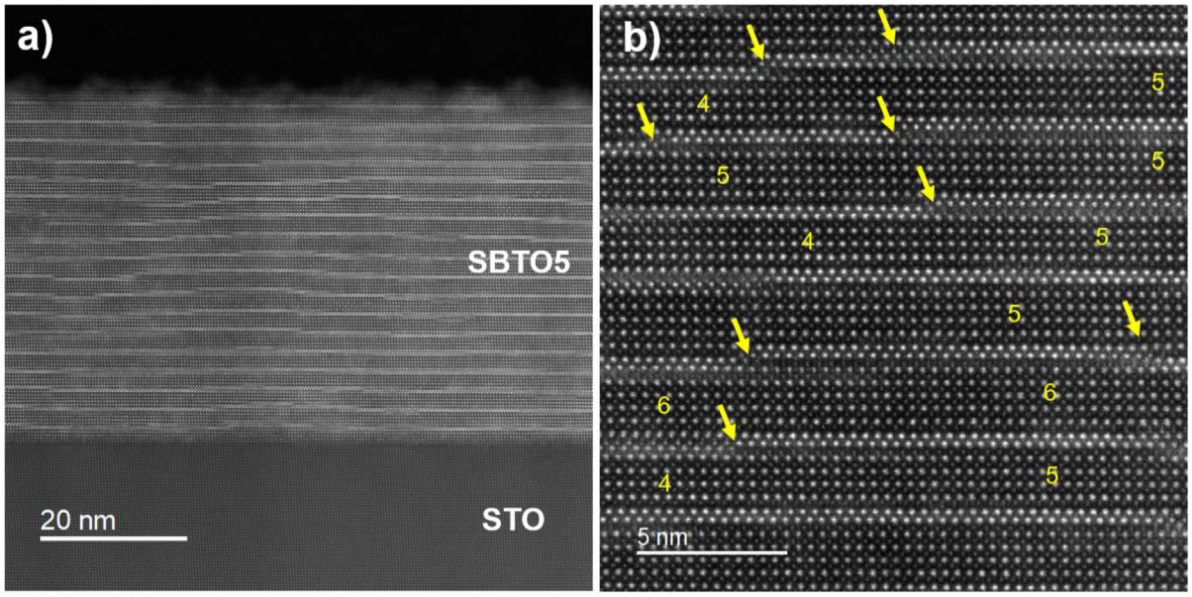

Figure 6. STEM-HAADF cross-section images of a film grown in optimal conditions using the 20 wt.% SBTO5 target and deposition temperature T_{dep} = 650 °C (sample SBTO5_20_F, see Table S1, Supporting Information), with a thickness of 46 nm: a) general overview including STO substrate; b) larger magnification image of the film. The arrows indicate stacking faults consisting of out-of-phase boundaries which correspond to a structure translation of one single perovskite block in the vertical *c*-axis direction. The image evidences regions with varying integer number of perovskite blocks around average $n = 5$.

cleanest remanent polarization signal, which is the thickest film (≈250 nm and $n_{av} = 4.8$), for the thermodynamic analysis of the temperature-dependent $P(E)$ data that leads to the derivation of the EC response as a function of temperature. Although this sample permitted slightly higher E field amplitudes, we have selected $E_0 = 150$ kV cm^{-1} as a suitable compromise between the achieved polarization values and the signal-to-noise ratio (Figure S8, Supporting Information). **Figure 8** displays the in-plane remanent

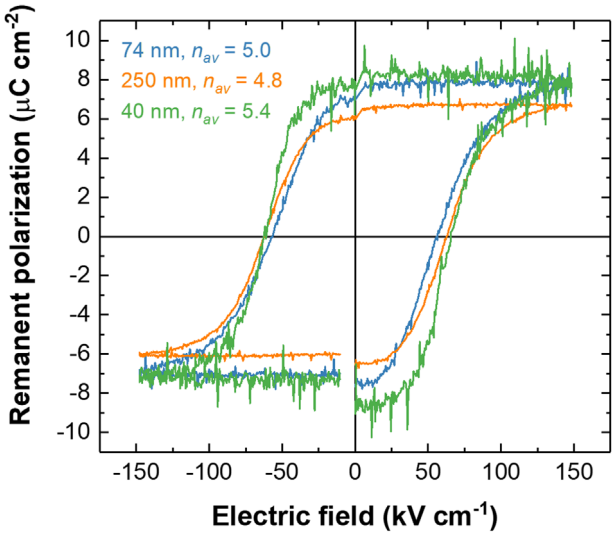

Figure 7. In-plane polarization versus electric field curves applying the remanent hysteresis protocol at room temperature for selected films grown using the 20 wt.% SBTO5 target having different thicknesses and average stacking order.

$P(E, T)$ data measured during heating, revealing a decreasing trend of polarization values with increasing temperature, as captured by the evolution of P_r as a function of temperature. Notably, even though P_r starts to decrease at ≈60 °C, it remains significantly above the zero-value characteristic of the paraelectric phase within the temperature range studied. This observation is consistent with the fact that the film is still far from reaching its ferroelectric Curie temperature ($T_C \sim 285$ °C for bulk SBTO5[23,24]).

The ECE figures of merit, ΔS and ΔT, obtained from applying Equations (1) and (3), respectively, to the remanent $P(E, T)$ data of the thickest film grown with the 20 wt.% target, are shown in **Figure 9** as a function of temperature and at various ΔE values: 10, 50, 100, and 150 kV cm^{-1}. The data indicate a noticeable upward trend in the $-\Delta S(T)$ and $\Delta T(T)$ dependences, suggesting that we are approaching a maximum around T_C that lies outside the temperature range accessible by our setup. This is consistent with the temperature evolution shown by P_r (Figure 8). Consequently, we observe the largest intrinsic ECE response at the upper limit of the examined temperature range, reaching $\Delta T \sim 0.95$ °C ($\Delta E = 150$ kV cm^{-1}) at ≈135 °C. We note that although the maximum temperature measured is still far from the $T_C \sim 285$ °C value of bulk SBTO5, due to the distribution of intergrowths the film likely exhibits a diffuse ferroelectric transition and thus a broader ECE response over temperature, which explains the relatively high value of ΔT at ≈135 °C.

3. Conclusion

We have successfully grown high-quality *c*-axis epitaxial films of the complex $n = 5$ SBTO5 Aurivillius phase on STO substrates by PLD. Using a ceramic SBTO5 target with a 20 wt.% Bi-excess, we achieved *c*-axis oriented films with remarkably good crystalline

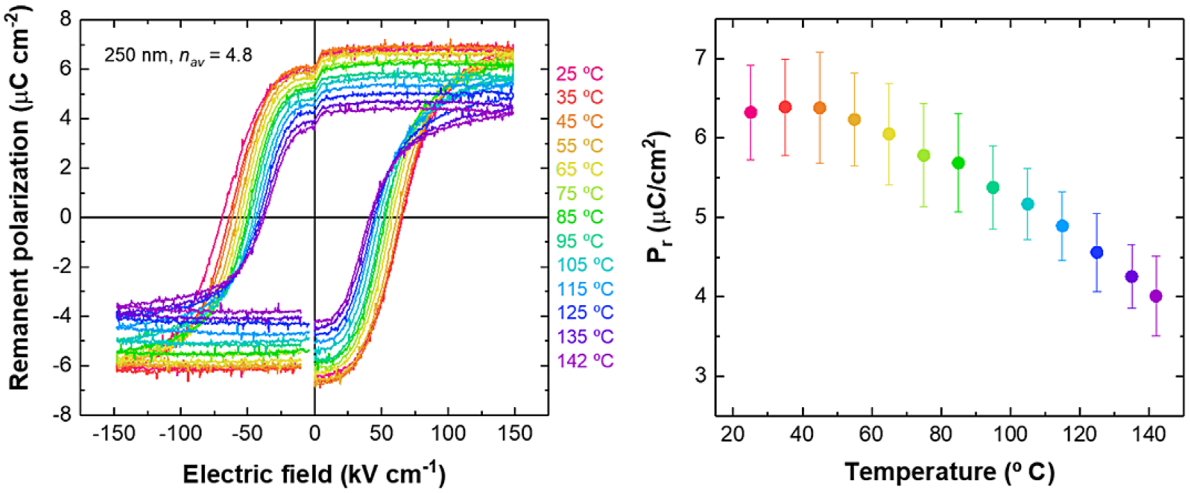

Figure 8. In-plane polarization versus electric field curves applying the remanent hysteresis protocol as a function of temperature upon heating for the thickest film grown using the 20 wt.% SBTO5 target (left) and evolution of the zero-field remanent polarization versus temperature from the same data (right).

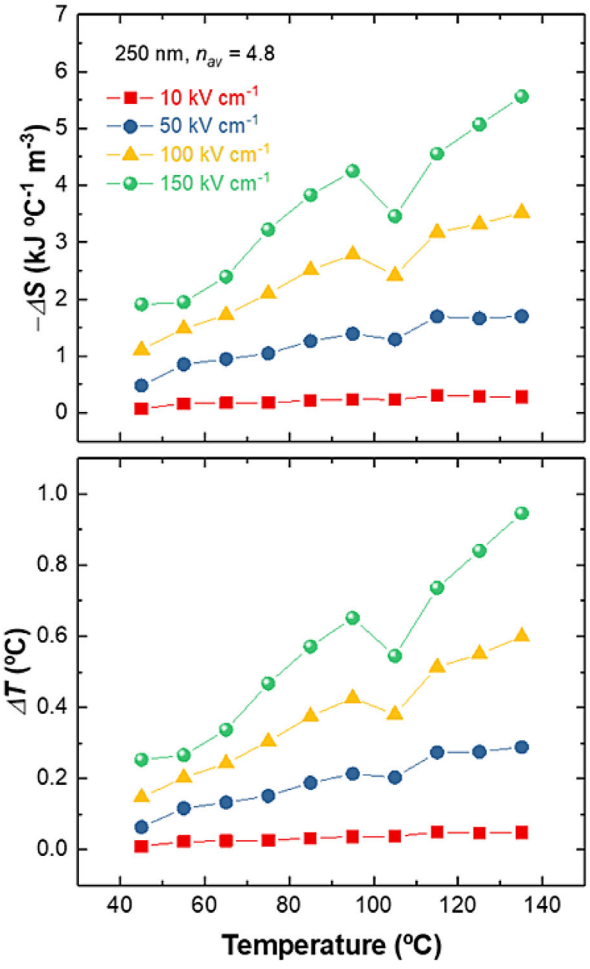

Figure 9. Isothermal entropy (top) and adiabatic temperature (bottom) variations of the electrocaloric effect as a function of temperature at various E field values, calculated from the in-plane remanent $P(E, T)$ data shown in Figure 8.

quality, closely aligning with the ideal $n = 5$ value at an optimal deposition temperature of 650 °C. To investigate the in-plane ferroelectric and EC properties, we utilized surface IDEs. By applying the remanent hysteresis protocol to measure the in-plane polarization, we were able to distinguish the film intrinsic ferroelectric response from the strong linear dielectric contribution of the STO substrate. This method provided P_r values ≈6–8 μC cm^{-2}, surpassing previously reported values for similar SBTO5 films using conventional bottom-top electrode configurations. Our results highlight the importance of selecting low-permittivity substrate materials to minimize their influence on the characterization of in-plane polarization in ferroelectric thin films when using IDEs. Additionally, we measured the film intrinsic polarization as a function of temperature, revealing a maximum ECE of $\Delta T \sim 0.95$ °C ($\Delta E = 150$ kV cm^{-1}) at ≈135 °C. Furthermore, we propose that the ECE could be further enhanced through modified compositions with lower T_C values, such as La/Nb codoped SBTO5, which has a T_C near room temperature in its bulk form. The epitaxial growth of such compositions could be pursued, using the optimized conditions established in this work as a foundation.

4. Experimental Section

Target Preparation: Dense ceramic pellets of SBTO5 prepared by the standard solid-state reaction method were used as Pulsed Laser Deposition (PLD) targets. Precursor powders of Bi_2O_3, $SrCO_3$, and TiO_2 with purities not less than 99.9% were used. Due to the high volatility of Bi, an excess of the Bi_2O_3 precursor weight with respect to the stoichiometric requirement was applied, and two different targets were prepared with 10 and 20 wt.% Bi-excess. The stoichiometric amounts (with the exception of the mentioned wt.% of Bi_2O_3 excess) were mixed and ground in a ball mill for 2 h. The powders were then calcined at 850 °C for 4 h. The resulting products were reground, pressed into pellets with 20 mm diameter under 10 Tons of uniaxial pressure, and sintered at 1190 °C for 4 h.

Thin Film Growth: SBTO5 thin films were grown by PLD on commercial (001)-oriented STO single crystal substrates of 5 × 5 × 0.5 mm^3 size (CrysTec GmbH). The substrates were cleaned sequentially in acetone,

ethanol and deionised water in an ultrasonic bath. The PLD processes were performed with a KrF excimer laser (248 nm, COMPex 102, Lambda Physik). The main experimental variables were the Bi-excess in the target (10 wt.% or 20 wt.% SBTO5) and the substrate deposition temperature T_{dep} (see Table S1, Supporting Information for a full list of samples). Other variables like oxygen partial pressure $P(O_2)$ or laser fluence were kept constant and the following common growth conditions were applied in the different films: 1) pre-ablation with 1000 pulses (same laser fluence as in the ablation, 10 Hz repetition rate) at room temperature, 2) heating at 20 °C min^{-1} up to the selected T_{dep} in a dynamic $P(O_2)$ of 100 mTorr, 3) ablation in the same $P(O_2)$ with a laser fluence set at 1.3 J cm^{-2} and 5 Hz repetition rate, 4) annealing after deposition for 10 min with a $P(O_2)$ of 10 Torr, and 5) cooling down to room temperature at 5 °C min^{-1} in the same $P(O_2)$.

Structural and Morphological Characterization: The structural characterization of the films was performed by X-ray diffraction (XRD) $2\theta/\omega$ wide scans, X-ray reflectivity (XRR) and reciprocal space maps (RSMs) of selected asymmetric reflections, by using a four-circle X-ray diffractometer (Malvern-Panalytical X'pert Pro MRD) and standard Cu $K\alpha_{1,2}$ X-ray source with a parabolic mirror (for reciprocal space maps, a 2xGe(220) monochromator was added to the incident optics). A 2D array PIXcel detector was used. The topography of selected films was studied using atomic force microscopy (AFM) in contact mode (Keysight 5100) over different areas. The structure of the films was also analyzed by high-angle annular dark-field scanning transmission electron microscopy (HAADF-STEM) on a Fisher Spectra microscope operated at 200 kV. Cross-section lamellas were prepared by focused ion beam (FIB) on a SBTO5 film deposited under optimized conditions, with the cut oriented to show STO [100] zone axis.

Interdigital Electrodes: IDEs were fabricated by means of optical lithography in a 100 class clean room facility and metal evaporation, going through several steps as reported elsewhere.[44] The fabricated IDEs consist of a Cr(20 nm)/Au(150 nm) bilayer and the pattern has three bonding paths with several fingers each, so the central one can couple to either side paths allowing two electrode pairs per sample. The E field is given by $E = V/g$, being V the applied voltage value and g the gap between fingers, while the total electrode area can be approximated by $A \approx N \times l \times t$, where N is the number of spaces between fingers, l the effective length of the fingers and t the film thickness.[38–40] The used pattern has $g = 15$ µm and consists of 38 fingers per bonding path, with a finger length and width of 1200 µm and 15 µm, respectively. Regarding the in-plane orientation geometry, for simplicity, the IDEs were placed such that the E field direction is parallel/perpendicular to the substrate lateral edges (i.e., the STO [100] or [010] directions). Given that the Aurivillius films grow with the in-plane lattice parameter along the STO [110] direction (and/or their equivalent directions), this configuration is also convenient because it assures the detection of the in-plane polarization along the a-axis. Since STO is cubic, no in-plane anisotropy is expected with respect to the orientation of the a- and b-axis of the Aurivillius phase. Further details can be found in Figure S9 (Supporting Information).

Ferroelectric and Electrocaloric Properties: These properties were investigated by measuring the in-plane polarization using the IDEs with a 500 V-built-in ferroelectric tester (Precision Premier II model, Radiant Technologies). Hysteresis measurements were carried out based on a bipolar triangular wave excitation, and also remanent hysteresis measurements based on half triangular waves following the principle of the positive-up negative-down (PUND) method.[41] The frequency of the triangular wave excitation was set to 2 kHz for both measurement protocols. Temperature (T)-dependent polarization versus E field, $P(E, T)$ curves, were measured on heating in a dedicated homemade cell allowing a maximum temperature of 140 °C. Samples were immersed in a silicon oil bath during the polarization measurements to avoid electric discharges. The commonly used thermodynamic formulations based on Maxwell relations were applied to the $P(E, T)$ data to derive the adiabatic temperature variation ΔT characteristic of the ECE. As recommended in previous works,[45,46] only the upper branches with $E > 0$ were used for the calculations. A polynomial was fitted to the isothermal $P(E)$ curves so that all their data points occur at the same E field values, and then $P(E)$ at the set of measured T values was transposed to give $P(T)$ at the new set of E field values. Then, the derivative of P with respect to temperature was calculated from the experimental incremental values of polarization versus temperature (5–10 °C steps) at a given E value, and finally the analysis was completed through stepwise integration to derive the entropy variation of the ECE, namely,

$$\Delta S = \int_0^E \left(\frac{\partial P}{\partial T}\right)_{E'} dE' \quad (1)$$

for any field change $\Delta E = E - 0$ as it is the current case. The adiabatic temperature variation can be calculated as well, namely,

$$\Delta T = -\frac{1}{\rho}\int_0^E \frac{T(E)}{c_p(E)}\left(\frac{\partial P}{\partial T}\right)_{E'} dE' \quad (2)$$

where ρ is the density and c_p the heat capacity of the material. As generally adopted for practical ΔT calculations, both T and c_p are assumed E field independent.[46] Thus, Equation (2) can be simplified as

$$\Delta T \approx -\frac{T}{\rho c_p}\Delta S \quad (3)$$

The values $\rho = 6$ g cm^{-3} and $c_p = 0.4$ J g^{-1} K^{-1} were used based on results from the previous study in bulk SBTO5.[24] Despite that, c_p is both T and E field dependent, the adopted approach leads to a reasonable approximation of the ECE in the films, considering the weak dependence in the surveyed temperature range (25 – 142 °C) and the fact that it is far from the ferroelectric T_C value ($T_C \sim 285$ °C for bulk SBTO5[23,24]) where strong anomalies appear in $c_p(T)$.[46]

Supporting Information

Supporting Information is available from the Wiley Online Library or from the author.

Acknowledgements

S.L. acknowledges funding from the European Union's Horizon 2020 research and innovation program under the Marie Skłodowska-Curie grant agreement No. 101029019. This work was also supported by Ministerio de Ciencia, Innovación y Universidades (PID2021-124734OB-C21), "Severo Ochoa" Programme for Centres of Excellence in R&D (CEX2023-001286-S, CEX2023-001263-S and CEX2021-001214-S) and Diputación General de Aragón (E11-23R, E12-23R). D. G. acknowledges financial support from the Gobierno de Aragón through a doctoral fellowship. Authors would like to acknowledge C. Cosculluela from Unidad Técnica en Ingeniería de Microdispositivos (INMA) and R. Valero for the IDEs fabrication at the National Facility ELECMI ICTS, node "Laboratorio de Microscopías Avanzadas", through Servicio General de Apoyo a la Investigación from Universidad de Zaragoza. The authors also acknowledge the use of instrumentation as well as the technical advice provided by the Joint Electron Microscopy Center at ALBA (JEMCA) and funding from Grant IU16-014206 (METCAM-FIB) to ICN2 funded by the European Union through the European Regional Development Fund (ERDF), with the support of the Ministry of Research and Universities, Generalitat de Catalunya. J. S. acknowledges B. Mundet, F. Belarre and M. Rosado for the STEM images and FIB fabrication of the lamellas, as well as the financial support of the European Commission through the Horizon H2020 funding by H2020-MSCA-RISE-ID:101007825 –ULTIMATE-I. X. T. acknowledges financial support by Ministerio de Ciencia, Innovación y Universidades (PID2021-123276OB-I00).

Conflict of Interest

The authors declare no conflict of interest.

Data Availability Statement

The data that support the findings of this study are available from the corresponding author upon reasonable request.

Keywords

aurivillius oxides, epitaxial thin films, ferroelectricity, pulsed laser deposition, solid-state electrocaloric cooling

Received: December 23, 2024
Revised: March 14, 2025
Published online:

[1] T. Correia, Q. Zhang, *Electrocaloric Materials. New Generation of Coolers*, Springer, Berlin, Heidelberg **2014**.
[2] M. Otoničar, B. Dkhil, *Nat. Mater.* **2020**, *19*, 9.
[3] J. Shi, D. Han, Z. Li, L. Yang, S. G. Lu, Z. Zhong, J. Chen, Q. M. Zhang, X. Qian, *Joule* **2019**, *3*, 1200.
[4] A. Torelló, E. Defay, *Adv. Electron. Mater.* **2022**, *8*, 2101031.
[5] A. S. Mischenko, Q. Zhang, J. F. Scott, R. W. Whatmore, N. D. Mathur, *Science* **2006**, *311*, 1270.
[6] B. Peng, H. Fan, Q. Zhang, *Adv. Funct. Mater.* **2013**, *23*, 2987.
[7] J. Li, A. Torelló, V. Kovacova, U. Prah, A. Aravindhan, T. Granzow, T. Usui, S. Hirose, E. Defay, *Science* **2023**, *382*, 801.
[8] M. Valant, A. K. Axelsson, F. L. Goupil, N. M. N. Alford, *Mater. Chem. Phys.* **2012**, *136*, 277.
[9] Y. Sun, S. E. Shirsath, S. Zhang, D. Wang, *APL Mater.* **2023**, *11*, https://doi.org/10.1063/5.0165495.
[10] A. Barman, S. Kar-Narayan, D. Mukherjee, *Adv. Mater. Interfaces* **2019**, *6*, 1900291.
[11] A. Moure, *Appl. Sci.* **2018**, *8*, 62.
[12] C. A.-P. de Araujo, J. D. Cuchiaro, L. D. McMillan, M. C. Scott, J. F. Scott, *Nature* **1995**, *374*, 627.
[13] B. H. Park, B. S. Kang, S. D. Bu, T. W. Noh, J. Lee, W. Jo, *Nature* **1999**, *401*, 682.
[14] N. A. Benedek, J. M. Rondinelli, H. Djani, P. Ghosez, P. Lightfoot, *Dalt. Trans.* **2015**, *44*, 10543.
[15] V. V. Shvartsman, D. C. Lupascu, *J. Am. Ceram. Soc.* **2012**, *95*, 1.
[16] M. A. Zurbuchen, J. Lettieri, S. K. Streiffer, Y. Jia, M. E. Hawley, X. Pan, A. H. Carim, D. G. Schlom, *Integr. Ferroelectr.* **2001**, *33*, 27.
[17] X. Moya, S. Kar-Narayan, N. D. Mathur, *Nat. Mater.* **2014**, *13*, 439.
[18] F. Le Goupil, *Doctoral Dissertation*, Imperial College London, London **2013**.
[19] A. K. Axelsson, F. L. Goupil, M. Valant, N. M. N. Alford, *Acta Mater.* **2017**, *124*, 120.
[20] A. K. Axelsson, F. L. Goupil, M. Valant, N. M. N. Alford, *J. Eur. Ceram. Soc.* **2018**, *38*, 5354.
[21] M. Kashyap, V. Shrivastava, R. Mishra, *Phys. Status Solidi* **2021**, *258*, 2100266.
[22] H. Chen, T.-L. Ren, X.-M. Wu, Y. Yang, L.-T. Liu, *Appl. Phys. Lett.* **2009**, *94*, 182902.
[23] P. Ferrer, M. Algueró, J. E. Iglesias, A. Castro, *J. Eur. Ceram. Soc.* **2007**, *27*, 3641.
[24] S. Lafuerza, D. Gracia, J. Blasco, M. Evangelisti, *J. Alloys Compd.* **2024**, *983*, 173923.
[25] J. Zhu, W.-P. Lu, X.-Y. Mao, R. Hui, X.-B. Chen, *Jpn. J. Appl. Phys.* **2003**, *42*, 5165.
[26] S. T. Zhang, B. Yang, J. F. Webb, Y. F. Chen, Z. G. Liu, D. S. Wang, Y. Wang, N. B. Ming, *J. Appl. Phys.* **2002**, *92*, 4599.
[27] Ismunandar, T. Kamiyama, A. Hoshikawa, Q. Zhou, B. J. Kennedy, Y. Kubota, K. Kato, *J. Solid State Chem.* **2004**, *177*, 4188.
[28] K. Momma, F. Izumi, *J. Appl. Crystallogr.* **2011**, *44*, 1272.
[29] M. A. Zurbuchen, W. Tian, X. Q. Pan, D. Fong, S. K. Streiffer, M. E. Hawley, J. Lettieri, Y. Jia, G. Asayama, S. J. Fulk, D. J. Comstock, S. Knapp, A. H. Carim, D. G. Schlom, *J. Mater. Res.* **2007**, *22*, 1439.
[30] E. Gradauskaite, M. Campanini, B. Biswas, C. W. Schneider, M. Fiebig, M. D. Rossell, M. Trassin, *Adv. Mater. Interfaces* **2020**, *7*, 2000202.
[31] E. Gradauskaite, N. Gray, M. Campanini, M. D. Rossell, M. Trassin, *Chem. Mater.* **2021**, *33*, 9439.
[32] E. Gradauskaite, K. A. Hunnestad, Q. N. Meier, D. Meier, M. Trassin, *Chem. Mater.* **2022**, *34*, 6468.
[33] S. Zhang, J. Deliyore-Ramírez, S. Deng, B. Nair, D. Pesquera, Q. Jing, M. E. Vickers, S. Crossley, M. Ghidini, G. G. Guzmán-Verri, X. Moya, N. D. Mathur, *Nat. Mater.* **2024**, *23*, 639.
[34] V. Kovacova, S. Glinsek, S. Girod, E. Defay, *Sensors* **2022**, *22*, 4049.
[35] A. Barman, S. Chatterjee, C. Ou, Y. Yau Tse, N. Banerjee, S. Kar-Narayan, A. Datta, D. Mukherjee, *APL Mater.* **2021**, *9*, https://doi.org/10.1063/5.0039143.
[36] M. Burriel, G. Garcia, M. D. Rossell, A. Figueras, G. Van Tendeloo, J. Santiso, *Chem. Mater.* **2007**, *19*, 4056.
[37] Y. L. Cheng, Y. Wang, H. L. W. Chan, C. L. Choy, *Microelectron. Eng.* **2003**, *66*, 872.
[38] N. J. Kidner, Z. J. Homrighaus, T. O. Mason, E. J. Garboczi, *Thin Solid Films* **2006**, *496*, 539.
[39] C. H. Nguyen, R. Nigon, T. M. Raeder, U. Hanke, E. Halvorsen, P. Muralt, *J. Phys. D. Appl. Phys.* **2018**, *51*, 175303.
[40] R. Nigon, T. M. Raeder, P. Muralt, *J. Appl. Phys.* **2017**, *121*, 204101.
[41] J. T. Evans, *The Relationship between Hysteresis and PUND Responses*, Radiant Technologies, Inc., Pan American Fwy **2008**.
[42] S. T. Zhang, C. S. Xiao, A. A. Fang, B. Yang, B. Sun, Y. F. Chen, Z. G. Liu, N. B. Ming, *Appl. Phys. Lett.* **2000**, *76*, 3112.
[43] L. Wang, L. Y. Ding, S. T. Zhang, Y. F. Chen, Z. G. Liu, *Solid State Commun.* **2009**, *149*, 2061.
[44] E. Langenberg, L. Maurel, N. Marcano, R. Guzmán, P. Štrichovanec, T. Prokscha, C. Magén, P. A. Algarabel, J. A. Pardo, *Adv. Mater. Interfaces* **2017**, *4*, 1601040.
[45] X. Moya, E. Stern-Taulats, S. Crossley, D. González-Alonso, S. Kar-Narayan, A. Planes, L. Mañosa, N. D. Mathur, *Adv. Mater.* **2013**, *25*, 1360.
[46] Y. Liu, J. F. Scott, B. Dkhil, *Appl. Phys. Rev.* **2016**, *3*, 031102.